

# UC Berkeley

## UC Berkeley Previously Published Works

### Title

Cosmogenic-neutron activation of TeO<sub>2</sub> and implications for neutrinoless double- $\beta$  decay experiments

### Permalink

<https://escholarship.org/uc/item/9752n28h>

### Journal

Physical Review C - Nuclear Physics, 92(2)

### ISSN

0556-2813

### Authors

Wang, BS  
Norman, EB  
Scielzo, ND  
et al.

### Publication Date

2015-08-27

### DOI

10.1103/PhysRevC.92.024620

Peer reviewed

# Cosmogenic-neutron activation of $\text{TeO}_2$ and implications for neutrinoless double-beta decay experiments

B. S. Wang,<sup>1</sup> E. B. Norman,<sup>1,2</sup> N. D. Scielzo,<sup>2</sup> A. R. Smith,<sup>3</sup> K. J. Thomas,<sup>1,3</sup> and S. A. Wender<sup>4</sup>

<sup>1</sup>*Department of Nuclear Engineering, University of California, Berkeley, California 94720, USA*

<sup>2</sup>*Lawrence Livermore National Laboratory, Livermore, California 94550, USA*

<sup>3</sup>*Lawrence Berkeley National Laboratory, Berkeley, California 94720, USA*

<sup>4</sup>*Los Alamos National Laboratory, Los Alamos, New Mexico 87545, USA*

(Dated: September 18, 2018)

Flux-averaged cross sections for cosmogenic-neutron activation of natural tellurium were measured using a neutron beam containing neutrons of kinetic energies up to  $\sim 800$  MeV, and having an energy spectrum similar to that of cosmic-ray neutrons at sea-level. Analysis of the radioisotopes produced reveals that  $^{110\text{m}}\text{Ag}$  will be a dominant contributor to the cosmogenic-activation background in experiments searching for neutrinoless double-beta decay of  $^{130}\text{Te}$ , such as CUORE and SNO+. An estimate of the cosmogenic-activation background in the CUORE experiment has been obtained using the results of this measurement and cross-section measurements of proton activation of tellurium. Additionally, the measured cross sections in this work are also compared with results from semi-empirical cross-section calculations.

## I. INTRODUCTION

Neutrinoless double-beta ( $0\nu\beta\beta$ ) decay [1–3] is a long sought-after second-order weak process in which a nucleus ( $A, Z$ ) transitions to a nucleus ( $A, Z+2$ ) through the emission of two electrons. This process is hypothesized to occur only if neutrinos are Majorana particles. Observation of  $0\nu\beta\beta$  decay would not only establish that neutrinos are Majorana fermions, but may also constrain the neutrino-mass scale and hierarchy, and demonstrate that total lepton number is not conserved.

In experiments searching for  $0\nu\beta\beta$  decay, the signature of interest is a peak at the double-beta decay  $Q$  value ( $Q_{\beta\beta}$ ). As  $0\nu\beta\beta$  decay would be a rare process, minimizing the background rate around  $Q_{\beta\beta}$  is essential for improving the experimental sensitivity. Therefore, a detailed characterization of all potential sources of background is important, as any event that can mimic or obscure the  $0\nu\beta\beta$ -decay peak is problematic and must be well-understood and, if possible, eliminated.

To minimize external backgrounds,  $0\nu\beta\beta$ -decay experiments operate in underground laboratories, where large overburdens decrease the flux of cosmic rays by orders of magnitude relative to the flux above ground [4]. Further reduction of the remaining cosmic-ray background can be achieved with muon-veto detectors, and backgrounds from natural radioactivity in the laboratory environment can be alleviated with proper shielding.

Radioactivity present within the detector itself can provide a source of background that is difficult to eliminate.  $0\nu\beta\beta$ -decay experiments devote a great deal of effort into making ultraclean and ultrapure detector materials free of primordial radioisotopes. However, no matter how clean or purely produced the materials are, cosmogenic activation will generate some radioactivity while the materials are at or above the Earth's surface during storage, production, or transportation [5–7]. The background contribution from this radioactivity can be

minimized by ensuring detector materials spend as little time above ground as possible and by avoiding air transportation, as the cosmic-ray flux increases significantly at higher altitudes [8, 9]. At sea-level, activation is primarily caused by the hadronic component of the cosmic-ray flux, which is dominated by neutrons [10].

This work investigates the backgrounds associated with cosmogenic activation of tellurium, which are important to understand for experiments such as the Cryogenic Underground Observatory for Rare Events (CUORE) [11] and the Sudbury Neutrino Observatory Plus (SNO+) [12] that are searching for the  $0\nu\beta\beta$  decay of  $^{130}\text{Te}$ , but to date are poorly characterized due to a lack of data. As  $0\nu\beta\beta$ -decay experiments run for several years, typically only long-lived cosmogenic isotopes (i.e., that have half-lives of order a year or longer) with  $Q$  values near or greater than the  $^{130}\text{Te}$   $Q_{\beta\beta}$  of 2528 keV [13–16] will be potential sources of background at the  $0\nu\beta\beta$ -decay peak.

Determining the resulting cosmogenic-activation background contribution to a  $0\nu\beta\beta$ -decay experiment requires estimating the production rates of the radioisotopes in tellurium. Activation cross sections that span a wide range of neutron energies, from thermal up to several GeV, are therefore needed; however, experimentally-measured cross-section data is currently sparse. For neutron energies above 800 MeV, cross sections for neutron activation are expected to be approximately equal to those for proton activation, and can be estimated from existing experimental data for proton energies 800 MeV – 23 GeV [17–19]. In these proton measurements, two long-lived radioisotopes were observed that have the potential to contribute background at the  $0\nu\beta\beta$ -decay peak:  $^{110\text{m}}\text{Ag}$  and  $^{60}\text{Co}$ . Below 800 MeV, experimental data exists for activation of natural tellurium by  $\sim 1$ –180 MeV neutrons [20] and activation of individual tellurium isotopes by thermal to  $\sim 15$  MeV neutrons [21]; however, only a few reactions were measured, and no cross sections were reported for the production of  $^{60}\text{Co}$  and  $^{110\text{m}}\text{Ag}$ . To deal with the lack of experimental data, the background

from cosmogenic activation has been estimated in the past (as in Ref. [7]) using a combination of the aforementioned neutron and proton measurements and codes that either implement the semi-empirical formulae by Silberberg and Tsao (S&T) [22–24] (e.g., YIELDX [22–24], ACTIVIA [25]), or are based on Monte Carlo (MC) methods (e.g., CEM03 [26], HMS-ALICE [27], GEANT4 [28, 29]).

These estimates can be greatly improved with additional neutron-activation cross-section measurements below 800 MeV, which can also be used to benchmark the S&T and MC codes. A sample of natural- $\text{TeO}_2$  powder was irradiated at the Los Alamos Neutron Science Center (LANSCE) with a neutron beam containing neutrons with kinetic energies up to  $\sim 800$  MeV, and having an energy distribution that resembles the cosmic-ray neutron flux at sea-level. Following exposure, the  $\gamma$  rays emitted from the sample were measured in a low-background environment with a high-purity-germanium (HPGe) detector to determine the radioisotopes present. Based on these results, flux-averaged cross sections were obtained for several dozen isotopes.

The cross sections are used to investigate the impact cosmogenic activation will have on CUORE, a next-generation  $0\nu\beta\beta$ -decay experiment that will use an array of 988 high-resolution, low-background natural- $\text{TeO}_2$  bolometers to search for the  $0\nu\beta\beta$  decay of  $^{130}\text{Te}$ . In addition, the measured cross sections are compared with cross sections calculated using the ACTIVIA code. Details of this measurement and subsequent analysis are discussed below.

## II. EXPERIMENTAL METHOD AND DATA ANALYSIS

### A. Target

The target consisted of 272 g of natural- $\text{TeO}_2$  powder held within a cylindrical plastic container wrapped on all sides with 0.05 cm of cadmium to remove thermal neutrons. The front and back cadmium-layers were also used to monitor the neutron flux on either side of the target. Circular aluminum and gold foils were placed throughout the target to monitor the neutron flux as well. The target geometry is illustrated in Figure 1, and the details of each target component are listed in Table I.

### B. Neutron irradiation

The target was irradiated with neutrons from the LANSCE 30R beam line for 43 hours during February 25–27, 2012. At LANSCE, neutrons are generated from spallation reactions induced by an 800 MeV pulsed proton beam incident on a tungsten target. The 30R beam line, which is  $30^\circ$  to the right of the proton beam, has a neutron-energy spectrum that closely resembles the

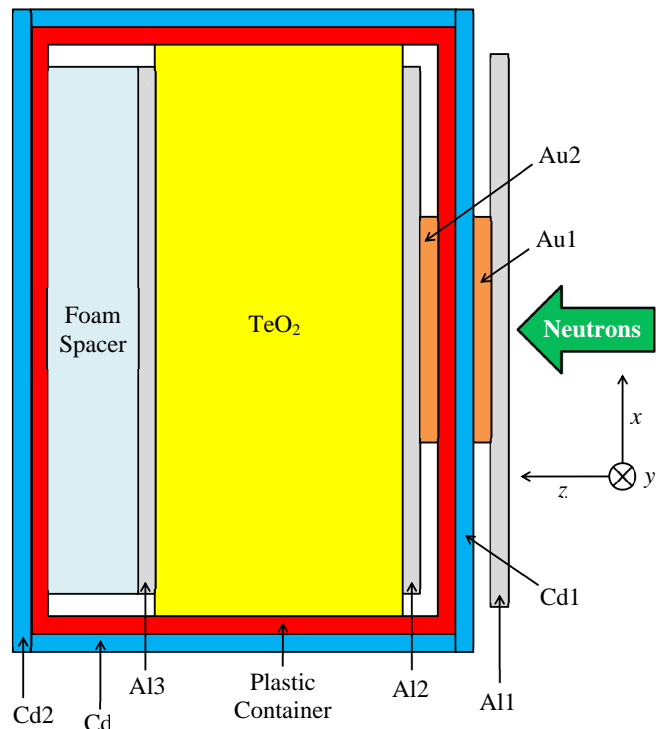


FIG. 1. Schematic of the target irradiated at LANSCE. The entire target is 6.2 cm long in the  $z$  direction. Each target component has cylindrical symmetry about the  $z$ -axis. This drawing is not to scale. Details on each component are given in Table I.

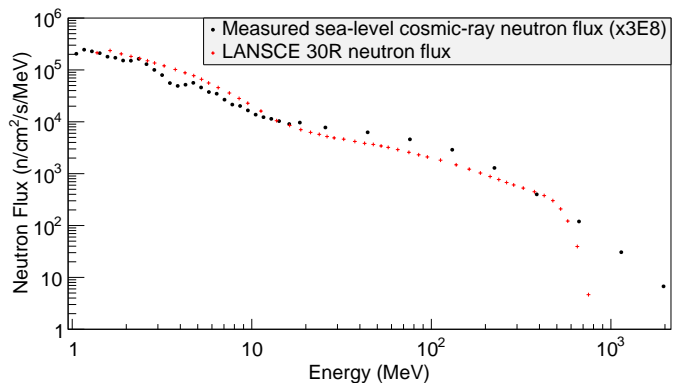


FIG. 2. LANSCE 30R neutron flux (red) [30] compared with the measured sea-level cosmic-ray-neutron flux (black) [31].

cosmic-ray neutron spectrum at sea-level, but has an intensity  $3 \times 10^8$  times larger, as shown in Figure 2. A beam collimation width of 8.26 cm was used, which resulted in a beam-spot diameter of 8.41 cm at the target.

The proton beam used to generate the neutrons consisted of 625- $\mu\text{s}$ -long macropulses occurring at a rate of 40 Hz. Each macropulse contained micropulses spaced 1.8  $\mu\text{s}$  apart. The neutron time-of-flight was obtained by measuring the time between the arrival of the proton

TABLE I. Description of the target components illustrated in Figure 1. The material, dimensions, mass, and purpose of each component are given. The parameters  $\Delta z$  and  $d$  are the thickness of the component along the z-axis and the diameter in the x-y plane, respectively.

Component	Material	$\Delta z$ (cm)	$d$ (cm)	Mass (g)	Purpose
TeO <sub>2</sub>	TeO <sub>2</sub> powder	2.79	6.43	271.56	Target
Al1	Al	0.0813	6.22	6.68	Neutron-flux monitor
Al2	Al	0.0813	5.93	6.06	Neutron-flux monitor
Al3	Al	0.0813	5.93	6.06	Neutron-flux monitor
Au1	Au	0.00515	2.54	0.504	Neutron-flux monitor
Au2	Au	0.00512	2.54	0.500	Neutron-flux monitor
Cd1	Cd	0.05	6.7	16.3	Neutron-flux monitor
					Thermal-neutron absorber
Cd2	Cd	0.05	7.3	19.9	Neutron-flux monitor
					Thermal-neutron absorber
Cd	Cd	0.05	—	—	Thermal-neutron absorber
Plastic Container	Polystyrene	0.2	—	—	Target holder

macropulse at the tungsten target and the generation of a fission signal in a  $^{238}\text{U}$ -fission ionization chamber [32] located 25.4 cm upstream of the TeO<sub>2</sub> target. The ionization chamber was only able to detect neutrons with energies above the  $^{238}\text{U}$ -fission threshold, which is approximately 1.25 MeV. The average neutron flux above 1.25 MeV at the TeO<sub>2</sub> target was determined to be  $1.41 \times 10^6$  neutrons/(cm<sup>2</sup>·s), with an estimated uncertainty of 10% [33] based on uncertainties in the geometry and efficiency of the ionization chamber.

### C. Gamma-ray analysis of the irradiated target

Approximately one week after the neutron irradiation, the TeO<sub>2</sub> target was dismantled, and each component was analyzed using  $\gamma$ -ray spectroscopy at the Lawrence Berkeley National Laboratory Low Background Facility [34, 35]. The TeO<sub>2</sub> powder, cadmium foils, and aluminum foils were measured using an upright, 115%-relative-efficiency, n-type HPGe detector, and the gold foils were measured with a horizontal, 80%-relative-efficiency, p-type HPGe detector. Each detector was surrounded by a copper inner shield encased in a lead outer shield. The gold foils were highly activated and could be counted at a distance of 12 cm from the detector. The cadmium and aluminum foils had low levels of activity and were therefore measured directly on top of the detector to maximize the detection efficiency. For the TeO<sub>2</sub> powder, the  $\gamma$ -ray measurements needed to be highly sensitive to long-lived radioisotopes, which had low levels of activity inside the powder. To maximize the detection efficiency, the TeO<sub>2</sub> powder was mixed thoroughly and counted in a Marinelli beaker positioned over the top of the detector (Figure 3). A plastic insert was placed inside the beaker to decrease the thickness and increase the height of the powder, which in turn increased the solid angle of the detector seen by the powder and decreased the self-attenuation of  $\gamma$  rays from decays within

the powder. The thickness and average height of the TeO<sub>2</sub> powder were 3.8 mm and  $\sim 5.6$  cm, respectively. The TeO<sub>2</sub> was counted in this configuration periodically for six months to enable the observation of long-lived activation products after the short-lived ones decayed away. Figure 4 shows a  $\gamma$ -ray spectrum for the TeO<sub>2</sub> powder collected four months after the irradiation.

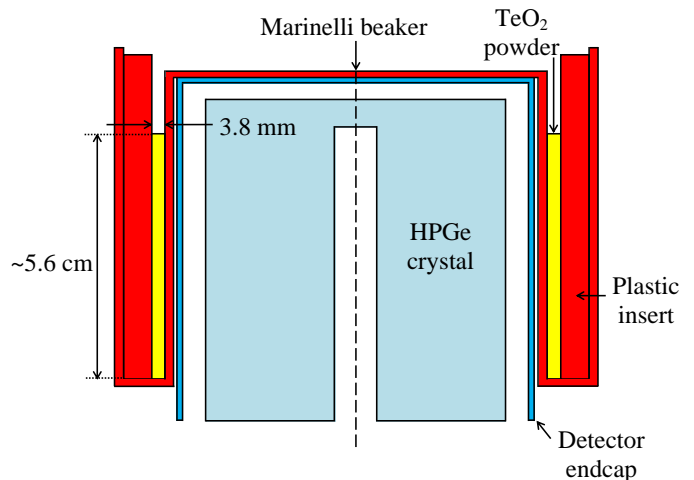


FIG. 3. Setup used during the  $\gamma$ -ray measurement of the TeO<sub>2</sub> powder. Each component has cylindrical symmetry about the dashed line. This drawing is not to scale.

Each peak in the  $\gamma$ -ray spectra was fit with a Gaussian summed with a quadratic background function to determine the energy and net counts. For peaks with higher intensity, a smoothed step function was also added to the fitting function. The  $\gamma$ -ray energies were used to identify the radioisotopes produced in the TeO<sub>2</sub> powder. For  $\gamma$ -ray lines that could come from the decay of more than one isotope, the contributors were identified from the decay half-life of the line.

A list of the radioisotopes observed in the TeO<sub>2</sub> powder

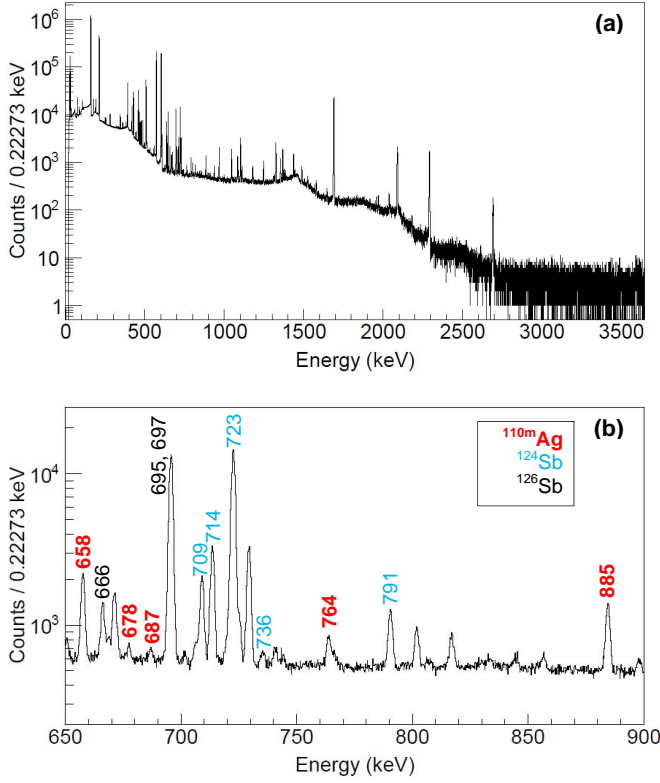


FIG. 4. 3-day-long  $\gamma$ -ray spectrum collected for the  $\text{TeO}_2$  powder four months after the neutron irradiation. (a) Full spectrum. (b) A region of the spectrum where  $^{110\text{m}}\text{Ag}$  peaks were observed. Labeled peaks are associated with the decay of isotopes with  $Q$  values greater than the  $Q_{\beta\beta}$  of  $^{130}\text{Te}$ , i.e.,  $^{110\text{m}}\text{Ag}$  (red and bolded),  $^{124}\text{Sb}$  (blue), and  $^{126}\text{Sb}$  (black). Other peaks in the region are from the decays of  $^{125}\text{Sb}$ ,  $^{129\text{m}}\text{Te}$ ,  $^{105}\text{Ag}$ , and  $^{114\text{m}}\text{In}$ .

is provided in Table II. Since  $\gamma$ -ray measurements started one week after the neutron irradiation ended, only activated isotopes with half-lives greater than  $\sim 1$  day remained. Therefore, any observed isotope with a shorter half-life was a decay daughter of a longer-lived isotope. For example, the presence of  $^{127}\text{Te}$  (9.35-hour half-life) and  $^{129}\text{Te}$  (69.6-minute half-life) was due to the decays of the longer-lived metastable states  $^{127\text{m}}\text{Te}$  and  $^{129\text{m}}\text{Te}$ , respectively.

#### D. Photopeak efficiencies

The  $\gamma$ -ray measurements of the  $\text{TeO}_2$  powder needed to be highly sensitive to long-lived radioisotopes, which had low levels of activity inside the powder. To maximize the detection efficiency, the powder was counted immediately next to the detector (Figure 3). Determination of the photopeak efficiencies for the  $\text{TeO}_2$  powder from calibration measurements alone was impractical due to the complexity of the counting geometry and the effects of true-coincidence summing, which can be significant at

such close range. Therefore, the efficiencies were obtained by running simulations with the Geometry and Tracking 4 (GEANT4) code, version 4.9.4.p02, which were benchmarked against experimental measurements of various point and extended  $\gamma$ -ray sources (Table III) that covered a wide range of  $\gamma$ -ray energies.

For the benchmarking measurements, the  $^{57}\text{Co}$  and  $^{54}\text{Mn}$  point sources were each counted at the center of the detector face and at four positions along the side of the detector that were spaced 2 cm apart and spanned the length of the HPGe crystal. The uranium source was counted on the side of the detector as well. Following the natural-source method [36], the two extended sources, ES1 and ES2, were constructed from powders that contained elements with naturally-occurring long-lived radioisotopes. ES1 was designed to mimic the geometry of the irradiated  $\text{TeO}_2$  powder during the  $\gamma$ -ray measurements, and ES2 was designed to mimic both the geometry and density of the powder. Photopeak efficiencies were obtained for all the  $\gamma$  rays listed in Table III. In addition, the total efficiency, which is needed to determine summing corrections, was obtained for the two  $^{57}\text{Co}$   $\gamma$  rays (122.06 keV and 136.47 keV) and the  $^{54}\text{Mn}$   $\gamma$  ray (834.85-keV).

The benchmarking measurements were simulated using GEANT4. Each simulation included the HPGe detector, the  $\gamma$ -ray source, and the lead and copper shielding. For each  $\gamma$  ray of interest, the entire decay scheme of the parent nucleus was simulated. Angular correlations between coincident  $\gamma$  rays were not taken into account; however at close distances to the detector, the effects on the photopeak efficiencies are largely averaged out and are thus small.

Each simulated photopeak or total efficiency ( $\epsilon_{s\gamma}$ ) was compared with the measured value ( $\epsilon_{m\gamma}$ ), and the percent difference was determined:

$$\Delta\epsilon_{\gamma} = \frac{\epsilon_{m\gamma} - \epsilon_{s\gamma}}{\epsilon_{s\gamma}} \times 100\%. \quad (1)$$

Using the manufacturer's detector specifications in the simulations resulted in  $\Delta\epsilon_{\gamma}$  values that ranged from approximately -10% to -35%, with the agreement between simulation and measurement worsening at lower  $\gamma$ -ray energies. This kind of disagreement, especially overestimation by the simulation, has been seen in other studies that model the  $\gamma$ -ray efficiencies of HPGe detectors using the geometry provided by the manufacturer (e.g., Refs. [37–40]). Typically, the discrepancies have been attributed to physical characteristics of the detector (crystal location, Li-diffused-contact thickness, etc.) that are difficult for the manufacturer to precisely specify. When the source is counted close to the detector, small uncertainties in the detector's parameters can have significant effects on the  $\gamma$ -ray efficiencies.

The adjustments listed in Table IV were applied to the detector geometry in GEANT4 to make the efficiencies from the simulations more closely match those from the

TABLE II. Radioisotopes observed in the irradiated TeO<sub>2</sub> powder. Unless otherwise indicated, all isotopes were produced by neutron interactions with tellurium. The measured and calculated flux-averaged cross sections ( $\bar{\sigma}_{30R}$  and  $\bar{\sigma}_{S\&T}$ , respectively) for neutron activation of tellurium are provided for isotopes with half-lives greater than 1 day. All  $\bar{\sigma}_{30R}$  were measured at the 68% C.L. and are independent cross sections, except for those followed by “(cu),” which are cumulative. All rows corresponding to isotopes that can contribute background at the <sup>130</sup>Te 0 $\nu\beta\beta$ -decay peak are bolded, and for these isotopes, the decay modes ( $\epsilon$  and  $\beta^-$  for electron capture and beta-minus decay, respectively) and Q values are given.

Isotope	Half-life	$\bar{\sigma}_{30R}$ (68% C.L.) (mb)	$\bar{\sigma}_{S\&T}$ (mb)	Decay Q value (MeV)
<sup>126</sup> I <sup>a</sup>	12.93 d			
<sup>131</sup> I <sup>a</sup>	8.025 d			
<sup>118</sup> Te	6.00 d	$5.7 \pm 1.2$	9.80	
<b><sup>119m</sup>Te</b>	<b>4.7 d</b>	<b><math>6.3 \pm 0.8</math></b>	<b>13.0</b>	<b>2.554 (<math>\epsilon</math>)</b>
<sup>121</sup> Te <sup>b</sup>	19.17 d			
<sup>121m</sup> Te	164.2 d	$16 \pm 2$	25.2	
<sup>123m</sup> Te	119.2 d	$36 \pm 4$	8.6	
<sup>125m</sup> Te	57.4 d	$83 \pm 10$	17.0	
<sup>127</sup> Te	9.35 h			
<sup>127m</sup> Te	106.1 d	$46 \pm 9$	25.3	
<sup>129</sup> Te	69.6 m			
<sup>129m</sup> Te	33.6 d	$53 \pm 17$ (cu)	22.4 (cu)	
<sup>131</sup> Te	25 m			
<sup>131m</sup> Te <sup>b</sup>	33.25 h			
<sup>131m</sup> Xe <sup>a</sup>	11.84 d			
<b><sup>118</sup>Sb</b>	<b>3.6 m</b>			<b>3.657 (<math>\epsilon</math>)</b>
<sup>119</sup> Sb <sup>c</sup>	38.19 h			
<b><sup>120m</sup>Sb</b>	<b>5.76 d</b>	<b><math>6.3 \pm 0.8</math></b>	<b>10.2</b>	<b><math>2.681 + E_{ex}</math> (<math>\epsilon</math>)</b>
<sup>122</sup> Sb	2.7238 d	$14 \pm 2$ (cu)	15.4 (cu)	
<b><sup>124</sup>Sb</b>	<b>60.2 d</b>	<b><math>16 \pm 2</math> (cu)</b>	<b>19.1 (cu)</b>	<b>2.904 (<math>\beta^-</math>)</b>
<sup>125</sup> Sb	2.759 y	$18 \pm 2$ (cu)	18.8 (cu)	
<b><sup>126</sup>Sb</b>	<b>12.35 d</b>	<b><math>6.7 \pm 0.9</math> (cu)</b>	<b>26.4 (cu)</b>	<b>3.673 (<math>\beta^-</math>)</b>
<sup>127</sup> Sb	3.85 d	$13 \pm 2$ (cu)	9.8 (cu)	
<sup>113</sup> Sn	115.1 d	$2.6 \pm 0.3$ (cu)	3.0 (cu)	
<sup>117m</sup> Sn	14 d	$4.3 \pm 0.6$	0.63	
<sup>111</sup> In	2.805 d	$2.3 \pm 0.3$ (cu)	2.1 (cu)	
<sup>114m</sup> In	49.51 d	$1.9 \pm 0.2$	0.31	
<sup>105</sup> Ag	41.29 d	$0.56 \pm 0.07$ (cu)	0.45 (cu)	
<b><sup>106m</sup>Ag</b>	<b>8.28 d</b>	<b><math>0.44 \pm 0.09</math></b>	<b>0.39</b>	<b>3.055 (<math>\epsilon</math>)</b>
<b><sup>110</sup>Ag</b>	<b>24.56 s</b>			<b>2.893 (<math>\beta^-</math>)</b>
<b><sup>110m</sup>Ag</b>	<b>249.83 d</b>	<b><math>0.28 \pm 0.04</math></b>	<b>0.054</b>	<b>3.010 (<math>\beta^-</math>)</b>
<sup>111</sup> Ag	7.45 d	$0.42 \pm 0.09$ (cu)	0.030 (cu)	
<sup>101</sup> Rh	3.3 y	$0.06 \pm 0.01$ (cu)	0.24 (cu)	
<sup>101m</sup> Rh	4.34 d	$0.30 \pm 0.05$ (cu)	0.24 (cu)	
<sup>102m</sup> Rh	3.742 y	$0.15 \pm 0.02$	0.12	
<b><sup>60</sup>Co<sup>d</sup></b>	<b>5.27 y</b>	<b><math>&lt; 0.0016</math> (cu)</b>	<b>0.0013 (cu)</b>	<b>2.823 (<math>\beta^-</math>)</b>
<sup>7</sup> Be <sup>e</sup>	53.24 d	$1.4 \pm 0.2$	2.5	

<sup>a</sup> This isotope was produced by interactions with spallation protons created in the target during the neutron irradiation. Therefore, no cross sections are provided.

<sup>b</sup> This isotope had a high probability of being produced by interactions with  $< 1.25$ -MeV neutrons. Therefore, no cross sections are given.

<sup>c</sup> A flux-averaged cross section could not be obtained for <sup>119</sup>Sb because the strongest  $\gamma$ -ray line at 24 keV overlapped with x-rays emitted by other activated isotopes.

<sup>d</sup> <sup>60</sup>Co was not conclusively observed in the  $\gamma$ -ray spectra due to <sup>102m</sup>Rh and <sup>110m</sup>Ag peaks being present where the <sup>60</sup>Co peaks were expected. Therefore the cross section quoted for <sup>60</sup>Co is an upper limit.

<sup>e</sup> <sup>7</sup>Be was produced almost exclusively by neutron interactions with oxygen. The cross sections given correspond to these interactions.

benchmarking measurements. The larger disagreement at low energies between the simulated and measured efficiencies pointed to additional, unspecified attenuating material that was present in the actual detector. To ad-

dress this, the thickness of the aluminum mounting cup that immediately surrounds the HPGe crystal was increased by 2.25 mm to achieve closer agreement between the simulations and measurements.

TABLE III. Description of  $\gamma$ -ray sources used to benchmark GEANT4.

Source	Composition	Dimensions	$\gamma$ -ray (keV)	Branching Ratio (%)
Co-57	Co-57	Point source	122.06 136.47	$85.60 \pm 0.17$ $10.68 \pm 0.08$
Mn-54	Mn-54	Point source	834.85	$99.9760 \pm 0.0010$
Uranium <sup>a</sup>	Natural uranium ore (0.1176 g) mixed with epoxy	Diameter = 4.76 cm Thickness = 3.175 mm	185.72 ( $^{235}\text{U}$ ) 46.54 ( $^{210}\text{Pb}$ ) 186.21 ( $^{226}\text{Ra}$ ) 242.00 ( $^{214}\text{Pb}$ ) 295.22 ( $^{214}\text{Pb}$ ) 1764.49 ( $^{214}\text{Bi}$ ) 2204.06 ( $^{214}\text{Bi}$ )	$57.2 \pm 0.8$ $4.25 \pm 0.04$ $3.64 \pm 0.04$ $7.251 \pm 0.016$ $18.42 \pm 0.04$ $15.30 \pm 0.03$ $4.924 \pm 0.018$
ES1 <sup>b</sup>	La <sub>2</sub> O <sub>3</sub> powder (89 g), Lu <sub>2</sub> O <sub>3</sub> powder (2 g), KCl powder (4 g)	Inner radius = 5.06 cm Outer radius = 5.443 cm Average height = 5.75 cm	201.83 ( $^{176}\text{Lu}$ ) 306.78 ( $^{176}\text{Lu}$ ) 788.74 ( $^{138}\text{La}$ ) 1435.80 ( $^{138}\text{La}$ ) 1460.82 ( $^{40}\text{K}$ ) 269.46 ( $^{223}\text{Ra}$ ) 271.23 ( $^{219}\text{Rn}$ ) 832.01 ( $^{211}\text{Pb}$ ) 351.07 ( $^{211}\text{Bi}$ )	$78.0 \pm 2.5$ $93.6 \pm 1.7$ $34.4 \pm 0.5$ $65.6 \pm 0.5$ $10.66 \pm 0.18$ $13.9 \pm 0.3$ $10.8 \pm 0.6$ $3.52 \pm 0.06$ $13.02 \pm 0.12$
ES2 <sup>b</sup>	(Unirradiated) TeO <sub>2</sub> powder (228 g), La <sub>2</sub> O <sub>3</sub> powder (23 g), Lu <sub>2</sub> O <sub>3</sub> powder (6 g), K <sub>2</sub> SO <sub>4</sub> powder (14 g)	Inner radius = 5.06 cm Outer radius = 5.443 cm Average height = 6.5 cm	Note: All $\gamma$ rays used to analyze ES1 were also used to analyze ES2.	

<sup>a</sup> All isotopes in the source were assumed to be in secular equilibrium.

<sup>b</sup> Due to a small  $^{227}\text{Ac}$  contamination in the La<sub>2</sub>O<sub>3</sub>, ES1 and ES2 also contained  $^{227}\text{Ac}$  and its daughter isotopes, which were assumed to be in secular equilibrium with each other.  $\gamma$ -rays from the  $^{227}\text{Ac}$  chain are also listed in the table.

Figure 5 shows the values of  $\Delta\epsilon_\gamma$  obtained after the adjustments to the detector geometry were made in the GEANT4 simulations. The uncertainties in  $\Delta\epsilon_\gamma$  take into account the statistical uncertainties in the measurements and the simulations, as well as the uncertainties in the source activities and branching ratios of the  $\gamma$  rays. The total uncertainty in the simulated efficiencies was estimated to be 5%, which is slightly larger than the standard deviation of  $\Delta\epsilon_\gamma$ .

The photopeak efficiencies of the  $\gamma$  rays used to identify the isotopes in Table II were obtained for the irradiated TeO<sub>2</sub> powder by performing GEANT4 simulations using the adjusted detector values in Table IV. Simulations indicate that summing could have as much as a 40% effect for certain photopeak efficiencies. Figure 5 gives confidence that the GEANT4 simulations could model summing correctly and provide photopeak efficiencies for the irradiated TeO<sub>2</sub> powder with around 5% uncertainty.

### E. Neutron transmission during neutron irradiation

Following the neutron irradiation, the aluminum and cadmium foils located in front of and behind the TeO<sub>2</sub> powder were measured with an HPGe detector, as was described in Section II C. The total neutron transmission,

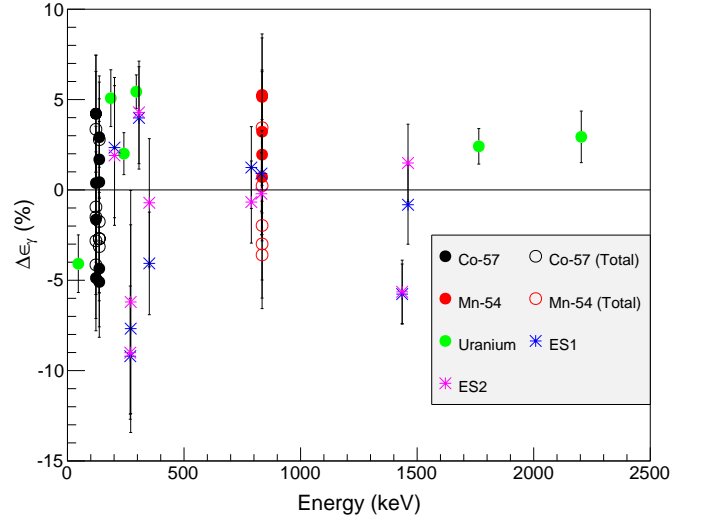


FIG. 5. Percent differences between the measured and simulated  $\gamma$ -ray efficiencies as a function of  $\gamma$ -ray energy. The simulated efficiencies were obtained using the adjusted values in Table IV. Points corresponding to total efficiencies are indicated with “(Total)” in the legend. All other points correspond to peak efficiencies.

$\bar{T}_{\text{tot}}$ , through the TeO<sub>2</sub> powder was estimated by comparing the activities of the activation products in the front

TABLE IV. Detector parameters adjusted in the GEANT4 simulations. The nominal values provided by the manufacturer are given, along with the values that allowed for satisfactory ( $\sim 5\%$ ) agreement between the efficiencies from the simulations and the benchmarking measurements.

Parameter	Nominal Value (mm)	Adjusted Value (mm)
Length of HPGe crystal	85.5	80.5 <sup>a</sup>
Distance between HPGe crystal and detector window	0	2
Thickness of aluminum mounting-cup	0.5	2.75
Thickness of internal dead layer (lithium contact)	1	2

<sup>a</sup> The effects of shortening the crystal in the simulation could also be reproduced by using the nominal length of the crystal and adding a 1.85-mm-thick, 3.5-cm-long copper ring around the aluminum mounting-cup, 8 cm below the top of the detector endcap. Since the presence of such a ring was not specified by the manufacturer and the corresponding simulations provided equivalent results to the shortened crystal geometry, the simulated efficiencies for the 80.5-mm-long crystal were used in the cross-section analysis.

TABLE V. Neutron-transmission results. Reactions used to determine the neutron transmission through the TeO<sub>2</sub> powder are listed, along with the corresponding values of  $\bar{T}_{\text{tot}}$ .

Reaction	$\bar{T}_{\text{tot}}$
$^{27}\text{Al}(n,X)^{22}\text{Na}$	$0.98 \pm 0.03$
$\text{Cd}(n,X)^{105}\text{Ag}$	$0.84 \pm 0.01$
$\text{Cd}(n,X)^{110\text{m}}\text{Ag}$	$0.86 \pm 0.01$

foils (Al1 and Cd1) with the activities in the back foils (Al3 and Cd2). The values of  $\bar{T}_{\text{tot}}$  obtained by analyzing the activation products are given in Table V, and the uncertainties quoted are statistical. To account for the variation in the results,  $\bar{T}_{\text{tot}}$  was taken to be  $0.90 \pm 0.10$ , which spans the range of values given in Table V along with their uncertainties. The average neutron transmission,  $\bar{T}$ , through the TeO<sub>2</sub> powder was then estimated to be

$$\bar{T} \simeq \frac{1 + \bar{T}_{\text{tot}}}{2} = 0.95 \pm 0.05. \quad (2)$$

#### F. Isotope-production rates

The production rate for each isotope can be determined using data from the  $\gamma$ -ray spectra collected for the irradiated TeO<sub>2</sub> powder. In most cases, the isotope produced in the powder is not fed by other isotopes during or after the neutron irradiation. Under this condition, the production rate,  $R_{30\text{R}}$ , can be obtained using:

$$R_{30\text{R}} = \frac{\lambda C_{\gamma}}{B_{\gamma} \epsilon_{\gamma}}, \quad (3)$$

where  $\lambda$  is the decay constant of the isotope,  $C_{\gamma}$  is the number of counts in the  $\gamma$ -ray peak of interest corrected for the growth and decay of the isotope during the irradiation and the decay of the isotope after the irradiation,

$B_{\gamma}$  is the branching ratio of the  $\gamma$  ray, and  $\epsilon_{\gamma}$  is the photopeak efficiency of detecting the  $\gamma$  ray. The production rates for  $^{125\text{m}}\text{Te}$  and  $^{127\text{m}}\text{Te}$  were described by more complex growth-and-decay relations and were obtained using the appropriate modifications to Equation 3.

#### G. Flux-averaged cross sections

The flux-averaged cross section,  $\bar{\sigma}_{30\text{R}}$ , for neutron activating an isotope in the irradiated TeO<sub>2</sub> powder is determined from

$$\bar{\sigma}_{30\text{R}} = \frac{\int_{E_{\text{min}}}^{E_{\text{max}}} \sigma(E) \varphi_{30\text{R}}(E) dE}{\int_{E_{\text{min}}}^{E_{\text{max}}} \varphi_{30\text{R}}(E) dE}, \quad (4)$$

where  $\sigma(E)$  is the cross section for producing the isotope with neutrons of kinetic energy  $E$ ,  $\varphi_{30\text{R}}(E)$  is the differential neutron flux hitting the front of the target in units of [neutrons/(cm<sup>2</sup>·s·MeV)], and  $E_{\text{min}}$  and  $E_{\text{max}}$  are respectively the lowest and highest neutron energies hitting the TeO<sub>2</sub> powder.

The isotope-production rate can also be expressed as

$$R_{30\text{R}} \approx N \bar{\sigma}_{30\text{R}} \bar{T} \int_{E_{\text{min}}}^{E_{\text{max}}} \varphi_{30\text{R}}(E) dE, \quad (5)$$

where  $N$  is the number of tellurium nuclei in the powder (except for the production of  $^7\text{Be}$ , where  $N$  is the number of oxygen nuclei in the powder).

The total neutron flux below 1.25 MeV during the irradiation was determined to be nonnegligible from the amount of  $^{198}\text{Au}$  created by (n, $\gamma$ ) reactions in the gold foils. Therefore, cross sections could be obtained only for isotopes produced solely (or primarily) by interactions with neutrons of energy  $> 1.25$  MeV, and in these cases,  $E_{\text{min}}$  and  $E_{\text{max}}$  from Equation 5 could be set to 1.25 MeV and 800 MeV, respectively.

The flux-averaged cross sections, shown in Table II, can then be determined from Equations 3 and 5.



### III. COMPARING MEASURED AND CALCULATED CROSS SECTIONS

Isotope-production cross sections for tellurium were also obtained by using the ACTIVIA code to perform calculations based on the S&T semi-empirical formulae. These formulae were originally developed to describe proton-nucleus interactions, but they are assumed to be applicable to neutron-nucleus interactions as well. The calculated cross sections are reported in Table II. Although the formulae are only valid for proton and neutron energies  $\geq 100$  MeV and they do not distinguish between ground and metastable states in product nuclei, the calculated and measured cross sections agree reasonably well, within a factor of 3 on average. One should note that the cross section calculated for  $^{110\text{m}}\text{Ag}$  was underestimated by approximately a factor of 5.

### IV. COSMOGENIC-ACTIVATION BACKGROUND IN THE CUORE EXPERIMENT

The CUORE experiment will use an array of 988 high-resolution, low-background  $\text{TeO}_2$  bolometers to search for the  $0\nu\beta\beta$  decay of  $^{130}\text{Te}$ . Each bolometer is comprised of a  $5\times 5\times 5$  cm<sup>3</sup> natural- $\text{TeO}_2$  crystal that serves as both a source and a detector of the decay. CUORE is aiming for a background rate of  $10^{-2}$  counts/(keV·kg·y) at the  $^{130}\text{Te}$   $Q_{\beta\beta}$  value of 2528 keV, which would allow the experiment to reach a half-life sensitivity of  $9.5\times 10^{25}$  years (90% C.L.), assuming a live time of 5 years and a full-width-at-half-maximum energy resolution of 5 keV [41].

Using the results of the neutron-activation measurement discussed in this work and the proton-activation measurements of Ref. [19], one can determine the background contribution to CUORE from the cosmogenic activation of the  $\text{TeO}_2$  crystals that occurs during sea transportation from the crystal-production site in Shanghai, China to LNGS in Italy. The results of both this work and Ref. [19] indicate that  $^{110\text{m}}\text{Ag}$  and  $^{60}\text{Co}$  are the only two long-lived radioisotopes that will contribute meaningfully to the background at the  $0\nu\beta\beta$ -decay peak due to their  $Q$  values being greater than  $Q_{\beta\beta}$ .  $^{110}\text{Ag}$  will also contribute a small amount to the background because  $^{110\text{m}}\text{Ag}$  decays to it 1.33% of the time.

The production rates,  $R$ , of  $^{110\text{m}}\text{Ag}$  and  $^{60}\text{Co}$  were each estimated to be

$$R \approx N \sum_i \sigma_i \phi_{\text{CR},i}, \quad (6)$$

where  $\sigma_i$  is the isotope-production cross section assigned to energy bin  $i$ , and  $\phi_{\text{CR},i}$  is the differential cosmic-ray neutron flux at sea-level integrated over energy bin  $i$ . The energy bins, integrated fluxes, and  $\sigma_i$  values are given in Table VI. The cosmic-ray neutron flux determined by Gordon *et al.* [31] was used in this analysis, with the

parameter  $F_{\text{BSYD}}$  from Ref. [31] taken to be  $0.73 \pm 0.22$  [33] for the route used to ship the  $\text{TeO}_2$  crystals. 80% of the  $^{110\text{m}}\text{Ag}$  and as much as 37% of the  $^{60}\text{Co}$  were produced by 1.25–800 MeV neutrons.

The fraction of  $^{110\text{m}}\text{Ag}$ ,  $^{110}\text{Ag}$ , and  $^{60}\text{Co}$  decays that deposit energy in a 60 keV-wide region-of-interest (ROI) surrounding the  $0\nu\beta\beta$ -decay peak was estimated using GEANT4 simulations of a single  $5\times 5\times 5$  cm<sup>3</sup>  $\text{TeO}_2$  crystal. The values obtained were 0.5%, 0.4%, and 1% for  $^{110\text{m}}\text{Ag}$ ,  $^{110}\text{Ag}$ , and  $^{60}\text{Co}$  decays, respectively. In the full CUORE array, the presence of nearby crystals would often lead to energy being deposited in more than one crystal. As most  $0\nu\beta\beta$ -decays would deposit all of their energy in a single crystal, the background can be reduced by rejecting events in which energy was deposited in more than one crystal. Simulations of a  $3\times 3\times 3$   $\text{TeO}_2$ -crystal array indicate that rejecting multi-crystal events can suppress the  $^{110\text{m}}\text{Ag}$  contribution to the ROI by a factor of  $\sim 2$ , while the contributions from  $^{110}\text{Ag}$  and  $^{60}\text{Co}$  will be minimally affected.

To estimate the background rate at  $Q_{\beta\beta}$  from cosmogenic activation of  $\text{TeO}_2$ , the following assumptions were made: (1) each crystal spends 3 months at sea level, (2) no  $^{110\text{m}}\text{Ag}$ ,  $^{110}\text{Ag}$ , and  $^{60}\text{Co}$  were present at the beginning of shipment due to their removal during the crystal-growth process, and (3) crystals were delivered to LNGS and stored underground at a constant rate from early 2009 to late 2013 [33]. The resulting contamination levels for  $^{110\text{m}}\text{Ag}+^{110}\text{Ag}$  and  $^{60}\text{Co}$  when CUORE begins operation in late 2015 will be  $\sim 2\times 10^{-8}$  Bq/kg and  $\sim 10^{-9}$  Bq/kg, respectively, which correspond to background rates of  $\sim 6\times 10^{-5}$  counts/(keV·kg·y) and  $\sim 7\times 10^{-6}$  counts/(keV·kg·y), respectively. After 5 years of running, the contamination levels will decrease to  $\sim 2\times 10^{-10}$  Bq/kg for  $^{110\text{m}}\text{Ag}+^{110}\text{Ag}$  and  $\sim 6\times 10^{-10}$  Bq/kg for  $^{60}\text{Co}$ , which correspond to background rates of  $\sim 4\times 10^{-7}$  counts/(keV·kg·y) and  $\sim 4\times 10^{-6}$  counts/(keV·kg·y), respectively. The contamination levels given here are lower than those predicted in Ref. [7] due to Lozza *et al.* assuming a longer exposure time of 1 year and a shorter overall cooling time underground of 2 years. Rejecting multi-site events should decrease the  $^{110\text{m}}\text{Ag}+^{110}\text{Ag}$  background rates by a factor of  $\sim 2$ . Although the background rates in the ROI are at least two orders of magnitude lower than the current CUORE goal background of  $10^{-2}$  counts/(keV·kg·y), for future experiments striving for essentially zero background, cosmogenic activation may have to be addressed more stringently.

### V. CONCLUSIONS

Flux-averaged cross-sections for cosmogenic-neutron activation of radioisotopes in natural tellurium were measured by irradiating  $\text{TeO}_2$  powder with a neutron beam containing neutrons of kinetic energies up to  $\sim 800$  MeV, and having an energy spectrum similar to that of cosmic-ray neutrons at sea-level. The cross sections obtained for

TABLE VI. Energy bins used in the estimation of the  $^{110\text{m}}\text{Ag}$  and  $^{60}\text{Co}$  production rates. The differential cosmic-ray neutron flux at sea-level integrated over each bin is provided. The isotope-production cross sections assigned to each bin are also listed. For bin 1, the cross sections obtained in this work are used. For bins 2, 3, and 4, the cross sections used were those measured in proton-activation experiments with 800 MeV, 1.4 GeV, and 23 GeV protons respectively. The individual contributions to  $R$  in units of  $[\text{s}^{-1}]$  and  $[\%]$  are given in the last two columns.

Bin	Bin Range	Integrated Neutron Flux ( $\text{s}^{-1}\cdot\text{cm}^2$ )	Cross section (mb)		Contribution to $R$ ( $\text{s}^{-1}$ )	
			$^{110\text{m}}\text{Ag}$	$^{60}\text{Co}$	$^{110\text{m}}\text{Ag}$	$^{60}\text{Co}$
1	1.25 MeV – 800 MeV	$(3.7 \pm 1.3) \times 10^{-3}$	$0.28 \pm 0.04$	$< 0.0016$	$(2.9 \pm 1.1) \times 10^{-6}$ (80%)	$< (1.7 \pm 0.6) \times 10^{-8}$ ( $< 37\%$ )
2	800 MeV – 1.4 GeV	$(5.3 \pm 1.9) \times 10^{-5}$	$3.95 \pm 0.40^{\text{a}}$ [42]	$0.09 \pm 0.04$ [19]	$(5.9 \pm 2.2) \times 10^{-7}$ (16%)	$(1.4 \pm 0.8) \times 10^{-8}$ ( $> 30\%$ )
3	1.4 GeV – 23 GeV	$(2.6 \pm 1.0) \times 10^{-5}$	$1.9 \pm 0.3$ [19]	$0.20 \pm 0.04$ [19]	$(1.4 \pm 0.6) \times 10^{-7}$ (3.9%)	$(1.5 \pm 0.6) \times 10^{-8}$ ( $> 33\%$ )
4	23 GeV – 150 GeV	$(1.6 \pm 0.6) \times 10^{-7}$	$0.88 \pm 0.59$ [19]	$0.75 \pm 0.08$ [19]	$(4.0 \pm 3.1) \times 10^{-10}$ (0.01%)	$(3.4 \pm 1.3) \times 10^{-10}$ ( $> 0.8\%$ )

<sup>a</sup> The value of this cross section was reported incorrectly in Ref. [19], but correctly in Ref. [42].

$^{110\text{m}}\text{Ag}$  and  $^{60}\text{Co}$ , the two isotopes which have both half-lives of order a year or longer and  $Q$  values larger than the  $Q_{\beta\beta}$  of  $^{130}\text{Te}$ , were combined with results from tellurium activation measurements with 800 MeV – 23 GeV protons to estimate the background in the CUORE experiment from cosmogenic activation of the  $\text{TeO}_2$  crystals. The anticipated  $^{110\text{m}}\text{Ag} + ^{110}\text{Ag}$  and  $^{60}\text{Co}$  background rates in  $[\text{counts}/(\text{keV}\cdot\text{kg}\cdot\text{y})]$  at the  $0\nu\beta\beta$ -decay peak were determined to be  $\sim 6 \times 10^{-5}$  and  $\sim 7 \times 10^{-6}$ , respectively, at the beginning of counting and  $\sim 4 \times 10^{-7}$  and  $\sim 4 \times 10^{-6}$ , respectively, after 5 years of counting. The  $^{110\text{m}}\text{Ag} + ^{110}\text{Ag}$  rates should decrease by a factor of  $\sim 2$  if multi-crystal events are efficiently rejected. These rates are at least two orders of magnitude lower than the goal background for the CUORE experiment.

## VI. ACKNOWLEDGEMENTS

We gratefully acknowledge the many valuable discussions with Maura Pavan and Silvia Capelli from the CUORE Collaboration. This work was supported by Lawrence Livermore National Laboratory under Contract DE-AC52-07NA27344, Los Alamos National Laboratory under Contract DE-AC52-06NA25396, Lawrence Berkeley National Laboratory under Contract DE-AC02-05CH11231, the U.S. Department of Energy Office of Defense Nuclear Nonproliferation (NA-22), the U.S. Department of Energy National Nuclear Security Administration under Award Number de-na0000979, and the Nuclear Forensics Graduate Fellowship from the U.S. Department of Homeland Security under Grant Award Number 2012-DN-130-NF0001-02. The views and conclusions contained in this document are those of the authors and should not be interpreted as necessarily representing the official policies, either expressed or implied, of the U.S. Department of Homeland Security.

[1] F. T. Avignone III, S. R. Elliot, and J. Engel, *Reviews of Modern Physics* **80**, 481 (2008).  
[2] W. Rodejohann, *International Journal of Modern Physics E* **20**, 1833 (2011).  
[3] S. M. Bilenky and C. Giunti, *Modern Physics Letters A* **27**, 1230015 (2012).  
[4] M. Aglietta, B. Alpat, E. D. Alyea, P. Antonioli, G. Badino, G. Bari, M. Basile, V. S. Berezinsky, F. Bersani, M. Bertaina, R. Bertoni, G. Bonoli, A. Bosco, G. Bruni, G. Cara Romeo, C. Castagnoli, A. Castellina, A. Chiavassa, J. A. Chinellato, L. Cifarelli, F. Cindolo, G. Conforto, A. Contin, V. L. Dadykin, A. De Silva,

M. Deutsch, P. Dominici, L. G. Dos Santos, L. Emaldi, R. I. Enikeev, F. L. Fabbri, W. Fulgione, P. Galeotti, C. Ghetti, P. Ghia, P. Giusti, R. Granella, F. Grianti, G. Guidi, E. S. Hafen, P. Haridas, G. Iacobucci, N. Inoue, E. Kemp, F. F. Khalchukov, E. V. Korolkova, P. V. Korchaguin, V. B. Korchaguin, V. A. Kudryavtsev, K. Lau, M. Luvisetto, G. Maccarone, A. S. Malguin, R. Mantovani, T. Massam, B. Mayes, A. Megna, C. Melagrana, N. Mengotti Silva, C. Morello, J. Moromisato, R. Nania, G. Navarra, L. Panaro, L. Periale, A. Pesci, P. Picchi, L. Pinsky, I. A. Pless, J. Pyrlík, V. G. Rjasny, O. G. Ryazhskaya, O. Saavedra, K. Saitoh, S. Santini, G. Sar-

- torelli, M. Selvi, N. Taborgna, V. P. Talochkin, J. Tang, G. C. Trinchero, S. Tsuji, A. Turtelli, I. Uman, P. Valania, G. Van Buren, S. Vernetto, F. Vetrano, C. Vigorito, E. von Goeler, L. Votano, T. Wada, R. Weinstein, M. Widgoff, V. F. Yakushev, I. Yamamoto, G. T. Zatsopin, and A. Zichichi, *Physical Review D* **58**, 092005 (1998).
- [5] S. Cebrián, J. Amaré, B. Beltrán, J. M. Carmona, E. García, H. Gómez, I. G. Irastorza, G. Luzón, M. Martínez, J. Morales, A. O. D. Solórzano, C. Pobes, J. Puimedón, A. Rodríguez, J. Ruz, M. L. Sarsa, L. Torres, and J. A. Villar, *Journal of Physics: Conference Series* **39**, 344 (2006).
- [6] S. R. Elliott, V. E. Guiseppe, B. H. Laroque, R. a. Johnson, and S. G. Mashnik, *Physical Review C* **82**, 1 (2010), arXiv:0912.3748.
- [7] V. Lozza and J. Petzoldt, (2014), arXiv:1411.5947.
- [8] W. N. Hess, H. Wade Patterson, and R. Wallace, *Physical Review* **116**, 445 (1959).
- [9] P. Goldhagen, J. M. Clem, and J. W. Wilson, *Radiation protection dosimetry* **110**, 387 (2004).
- [10] G. Heusser, *Annual Review of Nuclear and Particle Science* **45**, 543 (1995).
- [11] C. Arnaboldi, F. Avignone III, J. Beeman, M. Barucci, M. Balata, C. Brofferio, C. Bucci, S. Cebrian, R. Creswick, S. Capelli, L. Carbone, O. Cremonesi, A. de Ward, E. Fiorini, H. Farach, G. Frossati, A. Giuliani, D. Giugni, P. Gorla, E. Haller, I. Irastorza, R. McDonald, A. Morales, E. Norman, P. Negri, A. Nucciotti, M. Pedretti, C. Pobes, V. Palmieri, M. Pavan, G. Pessina, S. Pirro, E. Previtali, C. Rosenfeld, A. Smith, M. Sisti, G. Ventura, M. Vanzini, and L. Zanotti, *Nuclear Instruments and Methods in Physics Research Section A* **518**, 775 (2004).
- [12] J. Hartnell, *Journal of Physics: Conference Series* **375** (2012), arXiv:1742-6596/375/4/042015 [doi:10.1088].
- [13] M. Redshaw, B. Mount, E. Myers, and F. Avignone, *Physical Review Letters* **102**, 212502 (2009).
- [14] N. D. Scielzo, S. Caldwell, G. Savard, J. A. Clark, C. M. Deibel, J. Fallis, S. Gulick, D. Lascar, A. F. Levand, G. Li, J. Mintz, E. B. Norman, K. S. Sharma, M. Sternberg, T. Sun, and J. Van Schelt, *Physical Review C* **80**, 025501 (2009).
- [15] S. Rahaman, V.-V. Elomaa, T. Eronen, J. Hakala, A. Jokinen, A. Kankainen, J. Rissanen, J. Suhonen, C. Weber, and J. Äystö, *Physics Letters B* **703**, 412 (2011).
- [16] D. A. Nesterenko, K. Blaum, M. Block, C. Droese, S. Eliseev, F. Herfurth, E. Minaya Ramirez, Y. N. Novikov, L. Schweikhard, V. M. Shabaev, M. V. Smirnov, I. I. Tupitsyn, K. Zuber, and N. A. Zubova, *Physical Review C* **86**, 1 (2012).
- [17] D. W. Bardayan, M. T. F. da Cruz, M. M. Hindi, A. F. Barghouty, Y. D. Chan, A. Garcia, R.-M. Larimer, K. T. Lesko, E. B. Norman, D. F. Rossi, F. E. Wietfeldt, and I. Zliten, *Physical Review C* **55**, 820 (1997).
- [18] E. Norman, A. Smith, A. Barghouty, R. Haight, and S. Wender, *Nuclear Physics B - Proceedings Supplements* **143**, 508 (2005).
- [19] A. F. Barghouty, C. Brofferio, and S. Capelli, *Nuclear Instruments and Methods in Physics Research B* **295**, 16 (2013).
- [20] D. Hansmann, *About the Production of Residual Nuclides by Neutron-Induced Reactions up to 180 MeV*, Ph.D. thesis, Gottfried Wilhelm Leibniz Universität Hannover (2010).
- [21] N. Otuka, E. Dupont, V. Semkova, B. Pritychenko, A. Blokhin, M. Aikawa, S. Babykina, M. Bossant, G. Chen, S. Dunaeva, R. Forrest, T. Fukahori, N. Furutachi, S. Ganesan, Z. Ge, O. Gritzay, M. Herman, S. Hlavač, K. Kat, B. Lalremruata, Y. Lee, A. Makinaga, K. Matsumoto, M. Mikhaylyukova, G. Pikulina, V. Pronyaev, A. Saxena, O. Schwerer, S. Simakov, N. Soppera, R. Suzuki, S. Takács, X. Tao, S. Taova, F. Tárkányi, V. Varlamov, J. Wang, S. Yang, V. Zerkín, and Y. Zhuang, *Nuclear Data Sheets* **120**, 272 (2014).
- [22] R. Silberberg and C. H. Tsao, *The Astrophysical Journal Supplement Series No. 220(I)* **25**, 315 (1973).
- [23] R. Silberberg and C. H. Tsao, *The Astrophysical Journal Supplement Series No. 220(II)* **25**, 335 (1973).
- [24] R. Silberberg, C. H. Tsao, and A. F. Barghouty, *The Astrophysical Journal* **501**, 911 (1998).
- [25] J. Back and Y. Ramachers, *Nuclear Instruments and Methods in Physics Research Section A: Accelerators, Spectrometers, Detectors and Associated Equipment* **586**, 286 (2008).
- [26] S. G. Mashnik, a. J. Sierk, K. K. Gudima, and M. I. Baznat, *Journal of Physics: Conference Series* **41**, 340 (2006).
- [27] M. Blann, *Physical Review C* **54**, 1341 (1996).
- [28] S. Agostinelli, J. Allison, K. Amako, J. Apostolakis, H. Araujo, P. Arce, M. Asai, D. Axen, S. Banerjee, G. Barrand, F. Behner, L. Bellagamba, J. Boudreau, L. Broglia, A. Brunengo, H. Burkhardt, S. Chauvie, J. Chuma, R. Chytráček, G. Cooperman, G. Cosmo, P. Degtyarenko, A. Dell'Acqua, G. Depaola, D. Dietrich, R. Enami, A. Feliciello, C. Ferguson, H. Fesefeldt, G. Folger, F. Foppiano, A. Forti, S. Garelli, S. Giani, R. Giannitrapani, D. Gibin, J. Gómez Cadenas, I. González, G. Gracia Abril, G. Greeniaus, W. Greiner, V. Grichine, A. Grossheim, S. Guatelli, P. Gumplinger, R. Hamatsu, K. Hashimoto, H. Hasui, A. Heikkinen, A. Howard, V. Ivanchenko, A. Johnson, F. Jones, J. Kallenbach, N. Kanaya, M. Kawabata, Y. Kawabata, M. Kawaguti, S. Kelner, P. Kent, A. Kimura, T. Kodama, R. Kokoulin, M. Kossov, H. Kurashige, E. Lamanna, T. Lampén, V. Lara, V. Lefebvre, F. Lei, M. Liendl, W. Lockman, F. Longo, S. Magni, M. Maire, E. Medernach, K. Minamimoto, P. Mora de Freitas, Y. Morita, K. Murakami, M. Nagamatsu, R. Nartallo, P. Nieminen, T. Nishimura, K. Ohtsubo, M. Okamura, S. O'Neale, Y. Oohata, K. Paech, J. Perl, A. Pfeiffer, M. Pia, F. Ranjard, A. Rybin, S. Sadilov, E. Di Salvo, G. Santin, T. Sasaki, N. Savvas, Y. Sawada, S. Scherer, S. Sei, V. Sirotenko, D. Smith, N. Starkov, H. Stoecker, J. Sulkimo, M. Takahata, S. Tanaka, E. Tcherniaev, E. Safai Tehrani, M. Tropeano, P. Truscott, H. Uno, L. Urban, P. Urban, M. Verderi, A. Walkden, W. Wander, H. Weber, J. Wellisch, T. Wenaus, D. Williams, D. Wright, T. Yamada, H. Yoshida, and D. Zschesche, *Nuclear Instruments and Methods in Physics Research Section A* **506**, 250 (2003).
- [29] J. Allison, K. Amako, J. Apostolakis, H. Araujo, P. A. Dubois, M. Asai, G. Barrand, R. Capra, S. Chauvie, R. Chytráček, G. A. P. Cirrone, G. Cooperman, G. Cosmo, G. Cuttone, G. G. Daquino, M. Donszelmann, M. Dressel, G. Folger, F. Foppiano, J. Generowicz, V. Grichine, S. Guatelli, P. Gumplinger,

- A. Heikkinen, I. Hrivnacova, A. Howard, S. Incerti, V. Ivanchenko, T. Johnson, F. Jones, T. Koi, R. Kokoulin, M. Kossov, H. Kurashige, V. Lara, S. Larsson, F. Lei, O. Link, F. Longo, M. Maire, A. Mantero, B. Mascialino, I. McLaren, P. M. Lorenzo, K. Minamimoto, K. Murakami, P. Nieminen, L. Pandola, S. Parlati, L. Peralta, J. Perl, A. Pfeiffer, M. G. Pia, A. Ribon, P. Rodrigues, G. Russo, S. Sadilov, G. Santin, T. Sasaki, D. Smith, N. Starkov, S. Tanaka, E. Tcherniaev, B. Tomé, A. Trindade, P. Truscott, L. Urban, M. Verderi, A. Walkden, J. P. Wellisch, D. C. Williams, D. Wright, and H. Yoshida, *IEEE Transactions on Nuclear Science* **53**, 270 (2006).
- [30] “<http://wnr.lanl.gov>,”.
- [31] M. Gordon, P. Goldhagen, K. Rodbell, T. Zabel, H. Tang, J. Clem, and P. Bailey, *IEEE Transactions on Nuclear Science* **51**, 3427 (2004).
- [32] S. A. Wender, S. Balestrini, A. Brown, R. Haight, C. Laymon, T. Lee, P. Lisowski, W. McCorkle, R. Nelson, W. Parker, and N. Hill, *Nuclear Instruments and Methods in Physics Research A* **336**, 226 (1993).
- [33] B. S. Wang, *Cosmogenic Activation of TeO<sub>2</sub> in the Neutrinoless Double-Beta Decay Experiment CUORE*, Ph.D. thesis, University of California, Berkeley (2014).
- [34] K. J. Thomas, A. R. Smith, Y. D. Chan, E. B. Norman, B. S. Wang, and D. L. Hurley, *AIP Conference Proceedings* **1549**, 20 (2013).
- [35] “<http://lbf.lbl.gov>,”.
- [36] M. C. Perillo Isaac, D. Hurley, R. J. McDonald, E. B. Norman, and A. R. Smith, *Nuclear Instruments and Methods in Physics Research A* **397**, 310 (1997).
- [37] J. Boson, G. Ågren, and L. Johansson, *Nuclear Instruments and Methods in Physics Research A* **587**, 304 (2008).
- [38] N. Huy, D. Binh, and V. An, *Nuclear Instruments and Methods in Physics Research Section A* **573**, 384 (2007).
- [39] R. Helmer, J. Hardy, V. Iacob, M. Sanchez-Vega, R. Neilson, and J. Nelson, *Nuclear Instruments and Methods in Physics Research A* **511**, 360 (2003).
- [40] Z. Wang, B. Kahn, and J. Valentine, *IEEE Transactions on Nuclear Science* **49**, 1925 (2002).
- [41] F. Alessandria, E. Andreotti, R. Ardito, C. Arnaboldi, F. T. A. Iii, M. Balata, and I. Bandac, submitted to *Astroparticle Physics* (2011), arXiv:arXiv:1109.0494v2.
- [42] B. Quiter, *800 MeV Proton Irradiation of Neutrinoless Double Beta-Important Materials*, Masters thesis, University of California, Berkeley (2005).